

Molecular structure, vibrational spectra and first order hyperpolarizability of anilinium L-tartrate monohydrate (ALTM)

N. KANAGATHARA^a, M. K. MARCHEWKA^{b*}, G. ANBALAGAN^c, A. BEN AHMED^d, H. FEKI^d

^aDepartment of Physics, Jaya Engineering College, Chennai-602024

^bInstitute of Low Temperature and Structure Research, Polish Academy of Sciences, 50-422 Wroclaw, Poland

^cDepartment of Nuclear Physics, University of Madras, Guindy Campus, Chennai-600025.

^dLaboratory of Applied Physics, Faculty of Sciences 3018, BP 802 Sfax, Tunisia

Single crystals of anilinium L-tartrate monohydrate (ALTM) have been grown from slow solvent evaporation technique. The grown crystals have been subjected to single crystal X-ray diffraction and vibrational studies. Single crystal X-ray diffraction study confirmed that ALTM crystallizes in monoclinic system with non-centrosymmetric space group $P2_1$ (C2 in Schönflies notation). The geometrical parameters obtained by B3LYP method with 6-31G(d,p) basis set show good agreement with the observed value. The presence of various functional groups is identified by FT-IR and FT-Raman spectrum. The spectroscopic impacts of deuterated ALTM is also considered and discussed. The vibrational spectra have been examined on the basis of quantum chemical density functional theory (DFT) calculations using B3LYP/6-31G (d,p) approach. A detailed interpretation of the infrared spectra of ALTM was also reported. The HOMO-LUMO energy gap and other related molecular properties were discussed and reported. Stability of the molecule arising from hyperconjugative interactions and charge delocalization have been analysed by natural bonding orbital (NBO) analysis. Molecular electrostatic potential was also performed. To investigate microscopic second order non-linear optical behaviour of the examined complex, the electric dipole μ , the polarizability α and the hyperpolarizability β were computed using DFT/B3LYP/6-31G (d,p) method. According to our calculation, ALTM exhibits non-zero β value revealing microscopic second order NLO behaviour and it is found that second harmonic generation efficiency is 0.45 times that of KDP. Differential scanning calorimetric measurements have also been performed on the sample and discussed in detail.

(Received March 12, 2015; accepted April 6, 2017)

Keywords: Crystal structure, hydrogen bond, FT-IR, FT-Raman, Hyperpolarizability

1. Introduction

There is still interest in search for new non linear optical materials owing to their potential use in opto electronics and photonic devices [1]. The generation of coherent blue light through second harmonic generation from near infrared laser sources is an important technological problem that has attracted much attention in the last few years and its application lie in the fields of high density optical data storage, high resolution printing and spectroscopy [2,3]. Organic NLO materials have large optical susceptibilities, inherent ultrafast response times and high optical thresholds for laser power as compared with inorganic materials [4]. A number of organic materials with large dipole moment and a chiral structure linked through hydrogen bond have been reported in literature for their potential applications [5-7]. The tartaric acid is one such chiral molecule when combined with some organic bases exhibits noncentrosymmetric structures. The growth and other properties like thermal, dielectric, linear and nonlinear optical properties of anilinium D-tartrate was reported by Subhashini et al. [8] and many amino acid based tartrate salts with interesting properties like dielectric, piezoelectric, ferroelectric and

SHG were already published [9,10]. Also there are many promising tartrate derivatives crystallizes in noncentrosymmetric system and exhibits SHG [11-13]. Aniline is the simplest aromatic amine in which phenyl group is attached to amino group and has many industrial applications like dye, oil paints, rubber, pharmaceuticals and plastics. It also finds its applications in electronic conduction, electro luminescence and rechargeable batteries [14,15]. Recently considerable efforts have been made to combine amino acids with interesting organic matrices to produce materials having non centrosymmetric cell, large polarizability and a strong nonlinear optical coefficient [11,16-19]. ALTM belongs to the family of amino acid addition compounds which are known for their nonlinear optical properties. The hydrogen bonds between ions in ALTM is important for the preparation of solid-state materials prone to show second harmonic generation activity. This property makes ALTM to find its applicability in areas such as telecommunication, optical storage and information processing as well as mechanical energy transfer. The multidirectional hydrogen bonded tartrate anions provide a conformational rigid environment for the incorporation of anions to form SHG materials. To the best of our knowledge, experimental

data on geometric parameters and theoretical calculations on the structure of ALTM are not available in the literature. In this work, we report structural and vibrational spectroscopic study of ALTM in detail. The non-linear optical properties are also addressed theoretically. The electric dipole moment μ_{tot} , the isotropic polarizability α_{tot} and the first hyperpolarizability β_{tot} of ALTM are calculated. DSC study has also been performed for the first time.

2. Experimental

2.1. Crystal growth

The starting compounds, aniline (Aldrich, 99%) and L-tartaric acid (Aldrich, 94%) was used as supplied and prepared in the ratio 1:1. The saturated solution was prepared and cooled to room temperature, it remained clear, without any precipitants. Then, the solution was purified with the aid of active charcoal. The solution was slowly evaporated and within a few days the crystals appeared. The elemental analysis is consistent with the 1:1:1 composition of aniline: tartaric acid: water. Found: C: 46.71 %; H: 5.58 %; N: 5.34 %. Calculated for $(\text{C}_6\text{H}_8\text{N}) \times (\text{C}_4\text{H}_5\text{O}_6) \times (\text{H}_2\text{O})$: C: 45.98 %; H: 5.79 %; N: 5.36 %. The deuterated analogue was obtained by twofold recrystallization from D_2O , 99.2%). Crystals of as-grown ALTM is shown in Fig. 1.



Fig. 1. Photograph of ALTM crystal

2.2. Single crystal X-ray diffraction analysis

A colourless single crystal of ALTM having the edges of $0.38 \times 0.27 \times 0.23 \text{ mm}^3$ was used for the data collection on a four circle KUMA KM-4 diffractometer equipped with a two-dimensional area CCD detector. The graphite monochromatized $\text{MoK}\alpha$ ($\lambda = 0.71073 \text{ \AA}$) and ω -scan technique with $\Delta\omega = 0.75^\circ$ for one image were used for data collection. The 960 images for six different runs covering about 90% of the Ewald sphere were performed. Initially the lattice parameters were refined on 386 reflections obtained from 40 images for 8 runs with different orientation in the reciprocal space. Finally they

were refined by least-squares methods based on all measured reflections. One image was monitored as a standard for controlling the stability of the crystal after every 40 images. Integration of the intensities, correction for Lorentz and polarization effects was performed using KUMA KM-4 CCD software [20]. The face-indexed analytical absorption was calculated using the SHELXTL program [21], the maximum and minimum transmission factors being 0.6106 and 0.5426 respectively. A total of 4874 reflections were integrated (3562 independent reflections, $R_{\text{int}}=0.032$) and used for structure solution and refinement. The structure was solved by direct methods by use of SHELXL-97 program [22]. Initially the structure was refined with isotropic thermal parameters.

Table 1. Crystal data and structure refinement parameters for ALTM

Empirical formula	$\text{C}_4\text{H}_5\text{O}_6, \text{C}_6\text{H}_8\text{N}, \text{H}_2\text{O}$
Formula weight ($\text{g}\cdot\text{mol}^{-1}$)	261.23
Crystal system	Monoclinic
Space group	$P2_1$
$a(\text{\AA})$	9.615 (2)
$b(\text{\AA})$	7.316 (1)
$c(\text{\AA})$	17.311 (3)
β ($^\circ$)	96.47 (1)
Temperature (K)	295(2)
V (\AA^3)	1210.0 (4)
Z	4
λ Mo $K\alpha$ (\AA)	0.71073
D_{calc} (Mg m^{-3})	1.434
μ (mm^{-1})	0.12
$F(0\ 0\ 0)$	552
Crystal size (mm^3)	$0.38 \times 0.27 \times 0.23$
Crystal colour/habit	Colorless/ Parallelepiped
Θ range ($^\circ$)	3.0–27.0
h k l ranges	$-12 \rightarrow 13$; $-9 \rightarrow 7$; $-23 \rightarrow 23$
Reflections collected/unique	4874/ 3562 [$R_{\text{int}} = 0.032$]
Refinement method	Full-matrix least-squares on F^2
Data/Restraints/parameters	4874/0/ 386
$R[F^2 > 2\sigma(F^2)]$	0.042
$wR(F^2)$	0.118
Extinction coefficient	0.010 (3)
Largest difference peak and hole ($\text{e}\cdot\text{\AA}^{-3}$)	+ 0.26, -0.21

The hydrogen atoms were located from the difference Fourier maps, but in final refinement their positions were constrained using HFIX 43 with isotropic thermal

parameters of $1.2 U_{eq}$ of the nitrogen atoms joined directly to the hydrogen atoms (for H atoms of water molecules $U_{iso}=1.5U_{eq}$ of oxygen). In final refinement, all non-hydrogen atoms were refined with anisotropic thermal parameters by full-matrix least-squares methods by means

of SHELXL97 program. Details of the crystallographic data and final agreement factors are collected in the Table 1. Selected bond distances and angles are listed in Table 2. Table 3 gives the hydrogen bond parameters of ALTM.

Table 2. Comparison between observed and calculated geometric parameters of ALTM

Bonds distance (Å)			Bonds angles (°)		
Parameters	Observed	Calculated	Parameters	Observed	Calculated
O1-C1	1.246(3)	1.255	O1-C1-O2	127.3(2)	127.68
O2-C1	1.255(3)	1.266	O1-C1-C2	116.3(2)	114.07
O3-C4	1.294(3)	1.366	O2-C1-C2	116.40(19)	118.15
O4-C4	1.222(3)	1.206	O5-C2-C1	110.23(18)	110.66
O5-C2	1.423(3)	1.422	O5-C2-C3	109.94(18)	108.95
O6-C3	1.417(3)	1.425	C3-C2-C1	112.14(18)	108.37
C1-C2	1.544(3)	1.547	O6-C3-C2	109.47(18)	108.75
C2-C3	1.522(3)	1.554	O6-C3-C4	110.07(18)	110.55
C3-C4	1.525(3)	1.526	C2-C3-C4	108.83(18)	111.21
O11-C5	1.238(3)	1.270	O4-C4-C3	120.8(2)	125.99
O12-C5	1.257(3)	1.253	O4-C4-O3	125.2(2)	122.45
O13-C8	1.281(3)	1.329	O3-C4-C3	114.0(2)	111.53
O14-C8	1.207(3)	1.231	O11-C5-C6	117.3(2)	117.02
O15-C6	1.417(3)	1.419	O11-C5-O12	127.0(2)	126.88
O16-C7	1.406(3)	1.417	O12-C5-C6	115.7(2)	116.06
C5-C6	1.543(3)	1.544	O15-C6-C5	110.62(19)	105.18
C6-C7	1.528(3)	1.538	O15-C6-C7	111.01(18)	111.72
C7-C8	1.529(3)	1.527	C6-C7-C8	109.78(19)	112.20
N1-C11	1.478(3)	1.460	C7-C6-C5	111.65(18)	111.59
N2-C21	1.470(3)	1.464	O13-C8-C7	115.4(2)	112.60
C11-C12	1.360(3)	1.395	O14-C8-C7	119.4(2)	124.50
C12-C13	1.385(4)	1.394	O14-C8-O13	125.2(2)	122.87
C13-C14	1.358(4)	1.396	O16-C7-C6	110.1(2)	108.08
C14-C15	1.376(4)	1.395	O16-C7-C8	110.44(19)	110.87
C15-C16	1.384(4)	1.396	C11-C12-C13	118.7(3)	119.31
C16-C11	1.375(3)	1.394	C11-C16-C15	118.1(2)	118.75
C21-C22	1.353(3)	1.395	C12-C11-C16	122.1(2)	121.33
C21-C26	1.351(3)	1.393	C12-C11-N1	119.3(2)	118.84
C22-C23	1.390(4)	1.394	C13-C14-C15	119.9(3)	119.90
C23-C24	1.350(4)	1.396	C14-C13-C12	120.7(3)	120.09
C24-C25	1.371(4)	1.395	C14-C15-C16	120.5(3)	120.61
C25-C26	1.381(4)	1.396	C16-C11-N1	118.6(2)	119.82
			C21-C22-C23	118.9(2)	118.99
			C21-C26-C25	119.5(3)	118.56
			C22-C21-N2	118.8(2)	118.70
			C23-C24-C25	119.4(3)	119.99
			C24-C23-C22	120.8(3)	120.16
			C24-C25-C26	120.1(3)	120.57
			C26-C21-N2	120.0(2)	119.59
			C26-C21-C22	121.2(2)	121.70

Table 3. Hydrogen-bonding geometries of ALTM

D-H...A	D-H (Å)	H...A (Å)	D...A (Å)	D-H...A (°)
O3-H3O3...O2 ⁱ⁾	1.043	1.490	2.520	167.90
O5-H1O5...O1	0.789	2.030	2.599	128.83
O5-H1O5...O15	0.789	2.559	3.185	137.38
O6-H1O6...O1W ⁱⁱ⁾	0.879	1.840	2.705	167.20
O13-H13...O12 ⁱ⁾	1.119	1.380	2.492	171.50
O15-H1O5...O11	0.801	2.072	2.620	125.56
O15-H1O5...O1	0.801	2.321	2.933	133.80
O16-H1O6...O2W ⁱⁱⁱ⁾	0.882	2.088	2.924	157.70
N1-H1N1...O5 ^{iv)}	0.930	1.969	2.895	173.37
N1-H2N1...O2W ^{iv)}	0.916	1.946	2.852	169.58
N1-H3N1...O1 ^{v)}	0.912	1.891	2.791	168.51
N2-H1N2...O11 ^{v)}	0.943	1.838	2.775	171.69
N2-H2N2...O4 ^{iv)}	0.866	2.169	2.955	150.78
N2-H2N2...O6 ^{iv)}	0.866	2.408	3.099	137.07
N2-H3N2...O15 ^{v)}	0.954	1.953	2.904	174.16
O1W-H1O1...O6	0.902	1.978	2.861	165.71
O1W-H2O1...O4 ^{vi)}	0.870	1.874	2.728	167.10
O2W-H1O2...O14	1.014	1.646	2.645	167.70
O2W-H2O2...O16 ⁱ⁾	0.864	1.928	2.778	167.46

Symmetry codes: i) x, y+1, z; ii) -x, y+1/2, -z+1; iii) -x+1, y-1/2, -z+2;
iv) -x+1, y-1/2, -z+1; v) -x+1, y+1/2, -z+1; vi) x, y-1, z

2.3. Spectroscopic measurements

The vibrational measurements were carried out at room temperature. Infrared spectra were taken with a Bruker IFS-88 spectrometer in the region 4000-80 cm⁻¹ while powder Fourier Transform Raman (FT Raman) spectra in the region 3500-50cm⁻¹ were taken with an FRA-106 attachment to the Bruker IFS-88 spectrometer equipped with Ge detector cooled to liquid nitrogen temperature. Resolution was set up to 2 cm⁻¹, signal/noise ratio was established by 32 scans, weak apodisation. Nd³⁺:YAG air-cooled diode pumped laser of power ca. 200mW was used as an exciting source. The incident laser excitation is 1064 nm. The scattered light was collected at the angle of 180° in the region 3600-80 cm⁻¹, resolution 2 cm⁻¹, 256 scans. Due to the poor detector response, the Raman counterparts of the infrared bands located above 3200 cm⁻¹ are not observed in the spectrum presented. The polycrystalline powders were achieved by grinding in agate mortar with pestle. Samples, as suspensions in oil, were put between KBr wafers. The powder infrared spectra were taken in Nujol and Fluorolube emulsions to eliminate the bands originating from used oils.

2.4. Kurtz-Perry powder test

SHG experiment was carried out using Kurtz-Perry powder technique described in [23]. The calibrated samples (studied and KDP) were irradiated at 1064 nm by a Nd:YAG laser and the second harmonic beam power diffused by the powder sample (at 532 nm) was measured as a function of the fundamental beam power.

2.5. Differential scanning calorimetric measurements (DSC)

DSC was carried out on Perkin-Elmer DSC-7 calorimeter equipped with a CCA-7 low temperature attachment with a heating/cooling rate of 20°Cmin⁻¹. The sample of mass 9.924mg was sealed in the aluminium cap.

3. Computational details

The geometries were fully optimized without any constraint with the help of analytical gradient procedure implemented within Gaussian 98 program [24]. All the parameters were allowed to relax and all the calculations converged to an optimized geometry which corresponds to a true energy minimum revealed by the lack of imaginary values in the wave numbers calculations. Vibrational frequencies are calculated with B3LYP/6-31G (d,p) and then scaled by 0.963 [25]. Vibrational mode assignments were made by visual inspection of modes animated by using the Molekel program [26] and also with the results reported for similar compounds.

4. Results and discussion

4.1. Molecular geometry

Anilinium L-tartrate monohydrate [C₆H₈N. C₄H₅O₆. H₂O] (Fig. 1) crystallizes in monoclinic system with non-centrosymmetric space group P2₁ with four formula units

in unit cell ($Z = 4$). The cell dimensions are: $a = 9.615$ (2) Å, $b = 7.316$ (1) Å, $c = 17.311$ (3) Å, $\beta = 96.47^\circ$ and $V = 1210.0$ (4) Å³. Selected measured bonds lengths and bonds angles together with the calculated ones are grouped in Table 2. Figs. 2 and 3 show the molecular structure and packing diagram of ALTM. The asymmetric unit (Fig. 2) contains two L-tartaric acid anion ($C_4H_5O_6^-$), two aniline cations (C_6H_8N) and two molecules of water (H_2O) connected with N-H...O and O-H...O hydrogen bonds types. The anions of L-tartaric acid are connected through six O-H...O hydrogen bonds and form infinite chains. The anilinium cations are joined together via six N-H...O hydrogen bonds. The various hydrogen bond parameters are summarized in Table 3.

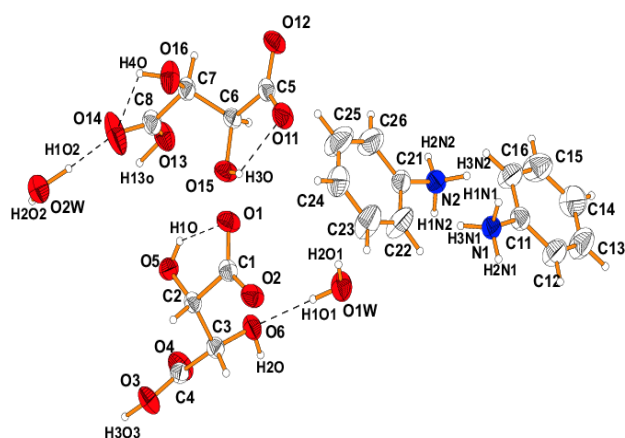


Fig. 2. Molecular structure of ALTM crystal with the labeling of the atoms

Fig. 4 shows the optimized structure of ALTM obtained by DFT-B3LYP method with 6-31G(d,p) basis set. The optimized geometric parameters obtained by B3LYP/6-31G (d,p) basis set are in well agreement with the experimental data and the largest discrepancies do not exceed 0.94 % for bonds lengths and 1.48 % for bonds angles. This discrepancies can be explained by the fact that the calculation relates to the isolated molecule where the intermolecular Coulombic interaction with the neighboring molecules are absent, whereas the experimental result corresponds to interacting molecules in the crystal lattice. The largest discrepancies between the calculated and experimental geometrical parameters are observed for X-H ($X = N, O$). Since large deviation from experimental X-H bonds may arise from the low scattering factors of hydrogen atoms in the X-ray diffraction experiment we did not discuss N-H and O-H bonds lengths.

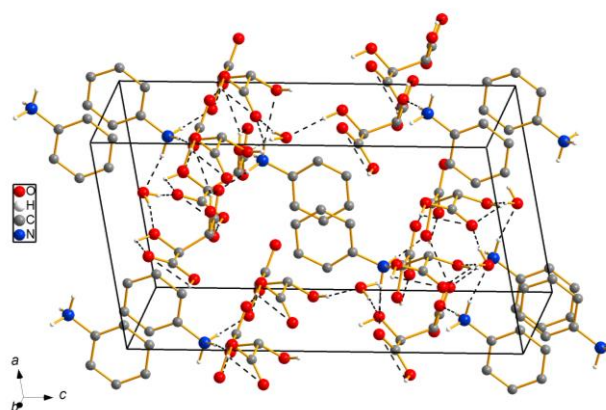


Fig. 3. Packing of the molecules in the unit cell. H atoms joined to C atoms are omitted for clarity. Dashed lines represent hydrogen bonds

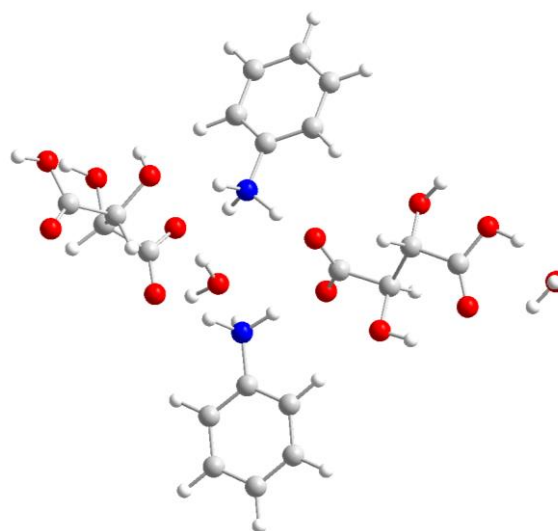


Fig. 4. Optimized structure of ALTM calculated at B3LYP/6-31G(d,p) basis set

4.2. Vibrational analysis

To the best knowledge of the authors, no papers were devoted to the vibrational properties of the ALTM crystal. The bands observed in the measured region $4000-400\text{ cm}^{-1}$ in FTIR spectrum and $3500-50\text{ cm}^{-1}$ in FT Raman spectrum arise from the vibrations of protons in the hydrogen bonds, the internal vibrations of the mono-protonated anilinium cations, tartrate anions and from the vibrations of the lattice. The vibrational spectra (IR and Raman) for protiated and deuterated ALTM crystals are shown in Figs. 5 and 6. The various functional groups viz C-C, C-N, N-H, C-H, C-O, C-O-H, COO⁻, O-H etc. and its vibrational band assignment is given in the Table 4.

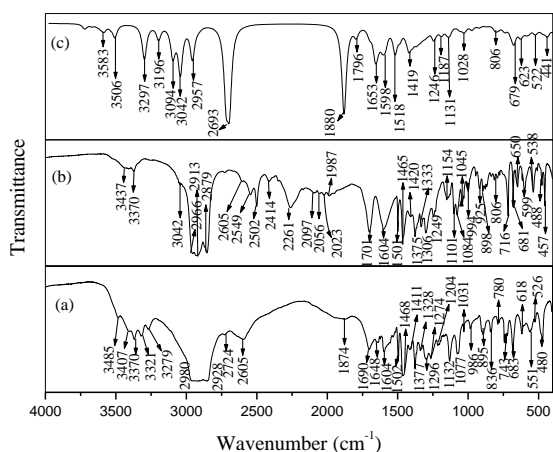


Fig. 5. FTIR spectrum of (a) protiated ALTM (b) deuterated ALTM (c) B3LYP/6-31G (d,p)

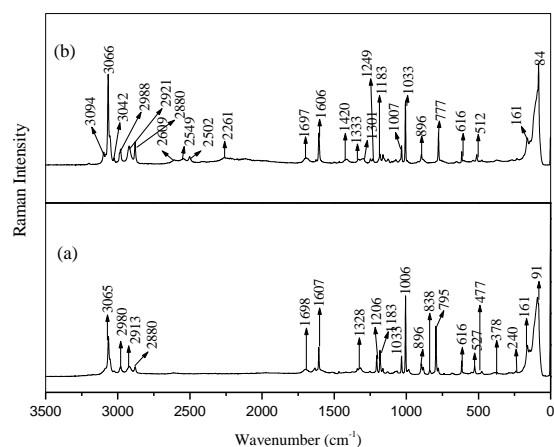


Fig. 6. FT Raman spectrum of (a) protiated ALTM (b) deuterated ALTM

Table 4. Experimental powder infrared and Raman spectra of ALTM crystal and its deuterated analogue

Frequency (cm ⁻¹)				Calculated Frequency cm ⁻¹	IR Intensity	Assignment
Protiated		Deuterated				
FT-IR	FT-Raman	FT-IR	FT-Raman			
3538vw		3524vwb		3671	48.17	O-H stretch (water)
3485w				3583	154.67	O-H stretch (Tartaric)
3407m		3406vw				O-H stretch (Tartaric)
3321m						NH ₃ asym stretch
3279m		3262vwb		3297	895.51	NH ₃ asym stretch
	3208		3200vw			N-H...O stretch
3189w	3166			3196	359.51	NH ₃ sym stretch
3143m						C-H stretch(benzene)
3118m						C-H stretch(benzene)
		3094vwb	3097vw	3094	78.34	C-H stretch(benzene) + NH ₃ sym stretch
3077m	3085vw	3074vw	3084vw	3089	3.64	C-H stretch(benzene) + NH ₃ sym stretch
	3065m	3065vw	3067vs	3066	0.42	C-H stretch(benzene)
3050m	3054w	3053vw	3055w			C-H stretch + O-H...O stretch
	3026vw	3025vw	3026vw			C-H stretch(tartaric)
3015m						C-H stretch(tartaric)
2980m	2980vw	2980vw	2981w			C-H stretch(tartaric)
2928m	2921vw		2921w	2934	25.22	C-H stretch(tartaric)
2910m		2913vw		2910	46.94	C-H stretch(tartaric)
2880m	2880vw	2879w	2880w	2891	7.11	N-H...O stretch
2853m						N-H...O stretch
2659m				2693	1853.71	N-H...O stretch
		2543m	2549vw			O-D stretch
		2500m	2502vw			O-D stretch
		2387w				O-D stretch
		2347w				O-D stretch
1874w				1880	2302.99	C-O-O ⁻ asym stretch
	1812vw			1794	254.08	C=O asym stretch
1690s	1698vw	1701vs	1697vwb	1698	208.85	C=O asym stretch
1648m				1653	361.66	NH ₃ asym def
1640m	1634vw			1642	23.14	NH ₃ asym def
1624m			1626vw	1615	145.49	H-O-H in plane def + NH ₃ asym def
1604s	1607m	1604vs	1606m	1601	76.21	H-O-H in plane def
1594s		1598vsb		1598	137.91	C-C stretch(benzene)

Frequency (cm ⁻¹)				Calculated Frequency cm ⁻¹	IR Intensity	Assignment
Protiated		Deuterated				
FT-IR	FT-Raman	FT-IR	FT-Raman			
1552m				1580	61.12	C-O-O ⁻ asym stretch
1532m						NH ₃ sym def + C-O-O ⁻ asym stretch
1516m	1513vw	1516m		1518	633.99	NH ₃ sym def
1502s						C-C stretch
1497s		1499vs	1501vw			C-C stretch
1495s		1492msh		1484	223.95	C-O stretch
1468m	1467vw	1465s	1465vw	1455	5.96	Ring stretch + C-H in plane bend
1411s	1419vw	1408s	1420vwb	1419	469.21	C-O-O ⁻ sym stretch
1377w	1373vw	1375vs		1393	235.67	C-H in plane bend+O-H in plane bend(tartaric)
		1359vs		1367	265.62	C-H in plane bend+O-H in plane bend(tartaric)
1340s	1340vw					C-H in plane bend+O-H in plane bend(tartaric)
1328m	1328vw	1333s	1333vw	1334	156.31	C-H in plane bend
	1318vw	1317s		1312	48.88	C-C stretch + O-H in plane bend
			1306vw			C-C stretch + O-H in plane bend
		1301vs	1301vw			C-C stretch + O-H in plane bend
1296s			1296vw	1296	67.41	C-C-H in plane bend + C-O-H in plane bend
1274s				1282	86.05	C-C-H in plane bend + C-O-H in plane bend
1266s						C-O stretch
1254ssh	1252vw	1247s	1249vw	1246	273.29	C-O stretch + O-H in plane bend + C-H out of plane
		1233s	1233vw			C-O stretch + O-H in plane bend + C-H out of plane
1216m				1224	63.97	C-H out of plane + O-H in plane bend
1204m	1206w	1205w		1206	16.58	C-C-H in plane bend+ O-H in plane bend
1195m				1192	30.93	Rock NH ₃
1178m	1183w		1183vw	1184	22.67	C-H (ring) in plane bend + C-N stretch
1169m				1166	0.58	Rock NH ₃ ⁺
1163m	1162vw		1162vw	1162	1.70	C-H (ring) in plane bend
		1151m	1154vw	1150	100.94	Rock NH ₃ ⁺ + C-H (ring) in plane bend
1136ssh		1141m		1142	40.10	C-H (ring) in plane bend
1132s	1130vw	1128m	1126vw	1131	188.58	C-O-H deformation
1106msh		1102s	1101vw			C-O-H deformation
1077s	1078vw	1079s	1073vw	1087	13.43	C-O stretch
1070s				1068	1.58	C-C-H in plane bend
	1065vw			1057	73.39	C-C stretch + C-O stretch
1031m	1033w	1031m	1033w	1028	93.05	C-C stretch + C-O stretch + O-H in plane bend
	1006vs	999w	1007s			C-C stretch + C-C-C in plane bend
	992vw		994vw			Ring deformation
986w		986w		981	1.66	Ring deformation
983w	984vw			977	92.75	C-H out of plane
938wb		942vw		946	0.22	C-H out of plane
904m						C-H out of plane
895m	896w	896w	896vw	898	0.73	C-H out of plane
883w	883vw	879w		880	7.28	C-C-O in plane bend + C-C stretch
843m				843	0.58	C-H out of plane bend(benzene)
836m	838	837vw		828	0.58	C-H out of plane bend(benzene)
	808vw	814w		806	143.24	O-H out of plane bend + C-C stretch (tartaric)
790w	795s	794w				C-N stretch

Frequency (cm ⁻¹)				Calculated Frequency cm ⁻¹	IR Intensity	Assignment
Protiated		Deuterated				
FT-IR	FT-Raman	FT-IR	FT-Raman			
780w	779vw	777vw	777m	787	40.25	C-N stretch + C-C-C in plane bend + O-H out of plane bend
743m	740vw	749vw		742	31.35	C-H out of plane bend (benzene) + C-O-C in plane bend
732m				735	40.76	C-H out of plane bend(benzene)
687msh				687	8.94	C-C-C out of plane bend
683s	684vw	681m		682	17.04	C-C-C out of plane bend
		650w	651vw	676	396.70	O-H out of plane bend
618m	616w	616w	616vw	627	106.60	O-H out of plane bend
603w		599w	602vw	587	112.28	O-C-O in plane bend
564m				571	91.45	O-C-O in plane bend
551wsh	548vw	538m	538vw	559	46.19	C-O-H out of plane bend
526w	527vw	510w	512vw	522	49.70	In plane ring def
493w		488w		490	10.86	Out of plane ring def
480m						Torsion NH ₃
476m	477vw	477w	477vw	477	60.21	C-N out of plane bend
472m				472	38.02	C-N out of plane bend
396w		390wsh		390	74.23	Rock H ₂ O
379m	378vw	369mb	374vwb	381	69.97	H-O-H out of plane bend
360w				360	64.13	Rock H ₂ O
324				331	7.90	C-C-O in plane bend
310wb				312	22.28	C-N out of plane bend
289w	288vw			289	42.98	Rock H ₂ O
273vw	272vw	274w		280	96.00	O-H out of plane bend
	240vw	233w	233vw			Torsion C-C-C-N
216vwb		203vw		210	119.20	bending N-H...O + bending O-H...O
166vw	161m	166w	161w	169	4.85	C-C-C in plane bend

4.2.1. N-H vibrations

According to crystallographic data, there are seven kinds of N-H...O type of hydrogen bonds with an average length of 2.895 Å. The vibrations of hydrogen manifest themselves as NH₃⁺ group vibrations of anilinium cation with weak interactions. ALTM show characteristics N-H stretching frequencies in the IR spectra, with a broad band in the region 3100-2800cm⁻¹ and multiple combination bands in the 2900-2000 cm⁻¹ which are characteristic IR bands of protonated amine salts [27]. In the region 3500-2200 cm⁻¹ there are overlapping of peaks due to O-H stretching of COOH and N-H stretching of NH₃⁺. The infrared absorption at 3321 and 3279 cm⁻¹ with medium intensity is assigned to NH₃⁺ asymmetric stretching of anilinium cation. The deuterated analogue of ALTM appears at 3262 cm⁻¹. The corresponding calculated infrared peak is at 3297 cm⁻¹ with strong intensity. NH₃⁺ symmetric stretching occurs at 3189 cm⁻¹ in infrared spectrum and its corresponding Raman counterpart occurs at 3166 cm⁻¹. The weak IR and Raman bands of deuterated analogue occurred at 3094 and 3097 cm⁻¹ may be assigned to NH₃⁺ symmetric stretching/C-H stretching of benzene. Similarly, the infrared peaks at 3077 and 3074 cm⁻¹ and Raman peaks at 3085 and 3084 cm⁻¹ with weak intensities are assigned to NH₃⁺ symmetric stretching/C-H stretching of benzene. The corresponding calculated PED is at 3094 cm⁻¹. The weak peaks at 476 and 477 cm⁻¹ in FTIR

and FT Raman is attributed to NH₃ torsional vibration. When an aliphatic amine is joined to a benzene ring through a carbon chain, both the characteristic amine band and the C-H deformation pattern will be present. In aniline, the characteristic broad band shown by aliphatic amine in the 830-730 cm⁻¹ region is not present, so that the out-of-plane C-H deformation of the benzene ring can be observed and these bands allow the ring substitution pattern to be determined [28]. The N-H in-plane bending vibration occurs at 1648 and 1640 cm⁻¹. The Raman peak occurs at 1634 cm⁻¹ with very weak intensity is ascribed to N-H in-plane bending vibration. The N-H out-of-plane bending vibration occurs at 1516 cm⁻¹ in IR and 1513 cm⁻¹ in Raman spectrum. Theoretically this peak occurs at 1518 cm⁻¹.

4.2.2. C-H vibrations

Aromatic compounds characteristics bands found in the five regions of the infrared spectrum viz. 3100-3000 cm⁻¹ (C-H stretching). 2000-1700 cm⁻¹ (overtone and combinations), 1650-1430 cm⁻¹ (C=C stretching), 1275-1000 cm⁻¹ (in-plane C-H deformation) and 900-690 cm⁻¹ (out-of-plane C-H deformation) [28]. In general, N-H and C-H vibrations are in the higher frequency region than C-O and C-N vibration. The carbon-hydrogen stretching occurs in the region 3100-3000cm⁻¹ and in this region the bands are not affected appreciably by the nature of the

substituent [29]. The medium IR peak at 3050 cm^{-1} and weak Raman peak at 3054 cm^{-1} are assigned to aromatic C-H stretching. The aliphatic C-H stretching gives IR absorptions at $3015, 2980, 2928, 2910\text{ cm}^{-1}$ and aliphatic C-H symmetric stretching gives contribution in Raman spectrum at $3026, 2980$ and 2921 cm^{-1} with weak intensity [30]. Here in the present study, this vibration attributed by 1468 cm^{-1} in IR and 1467 cm^{-1} in Raman spectrum. D atoms have the same characteristic vibrational motions as that of H atoms which includes C-D stretching, in-plane and out-of-plane bending vibrations. All these vibrations shifted to lower frequencies compared to the C-H vibrations because of the larger mass of the D atom. The incorporation of D instead of H molecules makes the C-D bond to be stronger than C-H bond as it occurs due to a result of lower zero-point energy. Hence the intensity of C-D vibrations should be no more than a few percent that of C-H vibrations [31]. Thus D substitution has impact on C-H stretching and bending features which is observed in deuterated spectrum of ALTM. The deuterated analogue IR/Raman peaks occurs at 1465 cm^{-1} with strong intensity. There are several peaks observed in the region $1377\text{-}1328\text{ cm}^{-1}$ and are attributed to C-H in-plane bending vibration and O-H in-plane bending vibration. The weak IR peak at 1163 cm^{-1} with Raman counterpart at 1162 cm^{-1} is assigned to C-H in-plane bending. This peak is shifted to lower wavenumbers 1151 and 1154 cm^{-1} in deuterated spectrum. C-H out-of-plane bending vibrations occur in the region $1000\text{-}700\text{ cm}^{-1}$. The weak IR and Raman peaks at 896 cm^{-1} is assigned to C-H out-of-plane bending vibration. The peaks observed in the region $983\text{-}836\text{ cm}^{-1}$ are assigned to C-H out-of-plane bending vibration. The medium infrared peak at 732 cm^{-1} is assigned to C-H out-of-plane bending and theoretically this value is at 735 cm^{-1} .

4.2.3. *COO⁻ and COOH vibrations*

Most organic compounds containing the C=O group show very strong infrared absorption in the range $1850\text{-}1650\text{ cm}^{-1}$. According to crystallographic data, both carboxyl groups of ALTM are ionized. The IR spectra clearly indicate the occurrence of proton transfer from the carboxylic acid to the amine molecules through reduction in the intensity of the carbonyl C=O stretching band in the $1675\text{-}1735\text{ cm}^{-1}$ region. The very strong infrared peak at 1690 cm^{-1} with very weak Raman counterpart at 1698 cm^{-1} is assigned to asymmetric stretching vibration of carbonyl groups. Usually this peak occurs at 1730 cm^{-1} . The reduction in this frequency number is due to complex formation of aniline and L-tartaric acid. The COO^- asymmetric stretching occurs at 1874 cm^{-1} with weak intensity in infrared and 1812 cm^{-1} in Raman spectrum. The asymmetric stretching of COO^- occurs at 1552 and 1532 cm^{-1} infrared with medium intensity. Theoretically this peak occurs at 1580 cm^{-1} . The symmetric stretching of COO^- occurs at 1411 cm^{-1} with strong intensity and its Raman at 1419 cm^{-1} . The alcoholic C-O stretching gives its contribution at $1296, 1274$ and 1254 cm^{-1} in FTIR spectrum with strong intensity. The corresponding

calculated PED occurs at 1296 and 1282 cm^{-1} . The Raman peak occurs at 1252 cm^{-1} with very weak intensity. The very strong IR band at 1132 cm^{-1} with Raman counterpart at 1130 cm^{-1} is due to in-plane bending of ionized carbonyl group. The strong infrared peak at 1077 cm^{-1} with very weak Raman peak at 1078 cm^{-1} is C-O stretching of tartaric acid. The C-O-H out-of-plane bending vibration contributes its mode at $551/548\text{ cm}^{-1}$ in IR/Raman spectrum.

4.2.4. *C-N vibrations*

It is very difficult to assign C-N stretching since mixing of several bands is possible in this region. Silverstein et al [32] assigned the C-N stretching absorption in the region $1382\text{-}1266\text{ cm}^{-1}$ for aromatic amines. Upon ionization of aniline, the C-N bond significantly shortens due to an increased conjugation between the planar NH_2 group and the ring. The medium infrared and Raman peak at $1178/1183\text{ cm}^{-1}$ is assigned to C-N stretching. The medium IR peak at $476, 472$ and 310 cm^{-1} with Raman peak at 477 cm^{-1} is assigned to C-N out-of-plane bending vibration. The C-N in-plane bending contributes its mode (IR/Raman: $166/161\text{ cm}^{-1}$) with weak intensity whereas C-N out-of-plane bending occurs at 477 cm^{-1} in infrared and Raman spectrum.

4.2.5. *C-C vibrations*

The C-C stretching occurs at 1594 cm^{-1} in IR with strong intensity. The strong infrared peak at 1502 cm^{-1} is assigned to C-C stretching of anilinium cation. The strong infrared peak at 1497 cm^{-1} with its weak Raman counterpart at 1501 cm^{-1} is assigned to C-C stretching of aniline ring. The strong IR peak at 1296 cm^{-1} is due to ring stretching of anilinium cation and usually this peak occurs at 1306 cm^{-1} . Now it changed their position due to self-association with intermolecular interactions. Experimental infrared spectrum shows strong peak at 1070 cm^{-1} which is assigned to C-C-H in-plane bending vibration. Its corresponding Raman peak occurs at 1065 cm^{-1} with very weak intensity. The very strong IR peak at 1006 cm^{-1} is due to C-C stretching or C-C-C in-plane bending vibration. The weak IR and Raman peaks at 780 and 779 cm^{-1} is due to C-C-C in-plane bending. The deuterated spectrum shows this ring vibration at 777 cm^{-1} . The strong IR peak occurs at 687 and 683 cm^{-1} is due to ring deformation. The infrared peaks at $603, 564, 551, 526$ and 493 are attributed to ring deformation.

4.2.6. *O-H vibration*

The hydroxyl groups are generally observed around 3500 cm^{-1} and this band is highly intense and broader than free OH vibration because of intermolecular hydrogen bonding. The broad and very weak infrared peak at 3538 cm^{-1} is due to O-H stretching vibration of water molecules. The weak infrared peaks at 3485 and 3407 cm^{-1} are due to O-H stretching of tartaric acid. The calculated PED shows this vibration at 3671 and 3583 cm^{-1} . The deuterated

spectrum of ALTM shows this vibration at 3524 and 3406 cm^{-1} with very weak intensities. The peaks observed in the region 2659- 2880 cm^{-1} are assigned to N-H...O stretching vibration. The stretching frequencies of O-D are lowered and occur in the region 2500-2300 cm^{-1} is due to the mass effect. Thus, IR peaks at 2543, 2500, 2387 and 2347 cm^{-1} with Raman peaks at 2549 and 2502 cm^{-1} in deuterated ALTM is attributed to O-D stretching. O-H in-plane bending occurs in the region 1420-1330 cm^{-1} . There are several peaks observed in the region 1377 – 1204 cm^{-1} and may assigned to C-H in-plane/out-plane bending as well as O-H in-plane bending vibration. The medium infrared peak at 1031 cm^{-1} and Raman peak at 1033 cm^{-1} is due to O-H in-plane bending vibration. The weak peaks around 630 cm^{-1} is due to O-H out-plane bending vibration.

4.3. Mulliken charge analysis

Mulliken charge is directly related to the vibrational properties of the molecule and quantifies how the electronic structure changes under atomic displacement; it is therefore related directly to the chemical bonds present in the molecule. The Mulliken charges affect the dipole moment, polarizability, electronic structure and more properties of molecular system. The Mulliken charge distribution of ALTM are calculated B3LYP /6-31G(d,p) basis set. The graphical charge distribution of ALTM is shown in Fig. 7. The charge distribution of the ALTM shows that all nitrogen atoms have maximum negative charges. Similarly all hydrogen atoms have positive charges. The hydrogen atoms which are involved in N-H...O, O-H...O interactions show higher positive values than other hydrogen atoms. Two carbon atoms C11 and C21 which are attached to the nitrogen atoms N1 and N2 of the aniline ring are positive and other carbon atoms (C12,C13,C14,C15,C16,C22,C23,C24,C25,C26) are negative. This may be due to the redistribution of the electron density in aniline molecule. All carbon atoms of tartaric acid have positive charges and the carbon atoms attached to the OH group (C2,C3,C6,C7) have less charge compared to the carbon atoms attached to COOH group (C1,C4,C5,C8). The charge distribution shows all the oxygen atoms of ALTM have negative charges. The increase in negative charges of oxygen atoms is observed for water molecules.

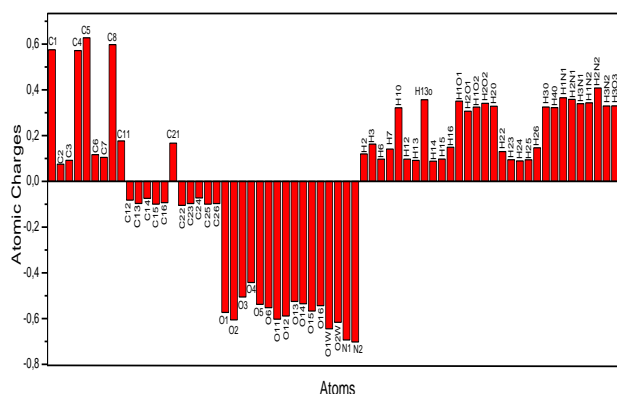


Fig. 7. Mulliken charge distribution of ALTM

4.4. Frontier molecular orbital analysis

Frontier molecular orbitals are important to determine properties such as molecular reactivity and the ability of a molecule to absorb light. It plays an important role in the electric and optical properties, as well as in UV-Vis spectra and chemical reactions [33,34].

The electronic transition from the ground state to the excited state is mainly described by an electron excitation from the highest occupied molecular orbital (HOMO) to the lowest unoccupied molecular orbital (LUMO). HOMO is an electron donor while LUMO is an electron acceptor that represents an ability to obtain electron. In-order to evaluate the energetic behavior of ALTM, we have carried out the calculations in gas phase by B3LYP /6-31G(d,p) basis set . The HOMO-LUMO energy gap of ALTM has been calculated and the HOMO-LUMO plot of ALTM is shown in Fig. 8. Both HOMO and LUMO is localized on the tartaric acid molecules and it is clear that there is no contribution of aniline in HOMO and LUMO. The separation between HOMO and LUMO is calculated as 3.78eV which indicates that charge transfer occurs within the molecule.

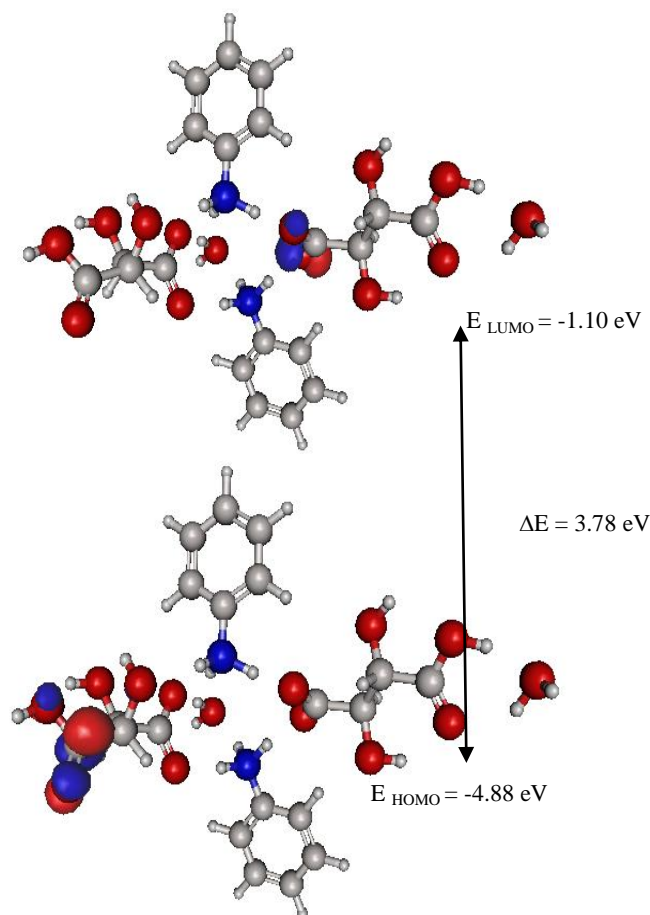


Fig. 8. Frontier molecular orbitals of ALTM

Global chemical reactivity descriptors of compounds such as hardness, chemical potential, softness, electro

negativity and electrophilicity index has been calculated and defined as follows

$$\eta = \frac{1}{2} \left(\frac{\partial^2 E}{\partial N^2} \right)_{v(r)} = \frac{1}{2} \left(\frac{\partial \mu}{\partial N} \right)_{v(r)} \quad (1)$$

$$\mu = \left(\frac{\partial E}{\partial N} \right)_{v(r)} \quad (2)$$

$$\chi = -\mu = - \frac{\partial E}{\partial N} \quad (3)$$

where E and $v(r)$ are electronic energy, external potential of an N -electron system respectively. Softness measures the extent of chemical reactivity. It is the reciprocal of hardness

$$S = \frac{1}{2\eta} \quad (4)$$

Using Koopman's theorem for closed-shell compounds μ , χ and S can be defined as,

$$\mu = \frac{I - A}{2} \quad \text{and} \quad (5)$$

$$\chi = \frac{I + A}{2} \quad (6)$$

where A and I are the ionization potential and electron affinity of the compounds respectively. Electron affinity refers to the capability of a molecule to accept precisely one electron from a donor. However in many kinds of bonding viz. covalent hydrogen bonding, partial charge transfer takes place. Recently Parr et al. [35] have defined a new descriptor to quantify the global electrophilic power of the compound as electrophilicity index (ω), which defines a quantitative classification of global electrophilic nature of a compound. Parr et al. have proposed electrophilicity index (ω) as a measure of energy lowering due to maximal electron flow between donor and acceptor. They defined electrophilicity index (ω) as follows.

$$\omega = \frac{\mu^2}{2\eta} \quad (7)$$

By taking into account the chemical hardness, HOMO-LUMO energy gap determines whether the molecule is hard or soft. Also the stability of the molecule can be related to hardness which means that the molecule having some energy gap means it is more reactive. The usefulness of this new reactivity quantity has been recently demonstrated in understanding the toxicity of various pollutants in terms of their reactivity and site selectivity [36,37]. All the calculated values of hardness, potential, softness and electrophilicity index are shown in Table 5.

Table 5. HOMO–LUMO energy value and related properties of ALTM calculated by B3LYP/6-31G(d,p) method

E_{HOMO} (eV)	-4.88
E_{LUMO} (eV)	-1.10 eV
Energy gap ΔE (eV)	-3.78
Ionization potential (A) eV	+4.88
Electron affinity (I)	+1.10
Global softness (S)	0.2645
Global hardness (η)	1.89
Chemical potential (μ)	2.99
Global electrophilicity (ω)	2.365

4.5. Density of states spectrum

In addition to the HOMO-LUMO energy levels, in the boundary region, neighbouring orbitals may show quasi degenerate energy levels [38,39]. In order to understand the molecular behavior completely, the total density of state spectrum of ALTM in terms of Mulliken population analysis were calculated and created by convoluting the molecular orbital information with Gaussian curves of unit height and full width at half maximum of 0.3 eV by using the Gauss sum 2.2 program [40]. The TDOS spectrum of ALTM is shown in Fig. 9 which gives the pictorial representation of MO (molecule orbital) compositions and their contributions to chemical bonding through the positive and negative charges. In general, positive value of DOS indicates a bonding interaction, negative value means that there is an anti-bonding interaction and zero value indicates nonbonding interactions [41]. Here in the present study, negative value indicates anti-bonding interaction between the molecules.

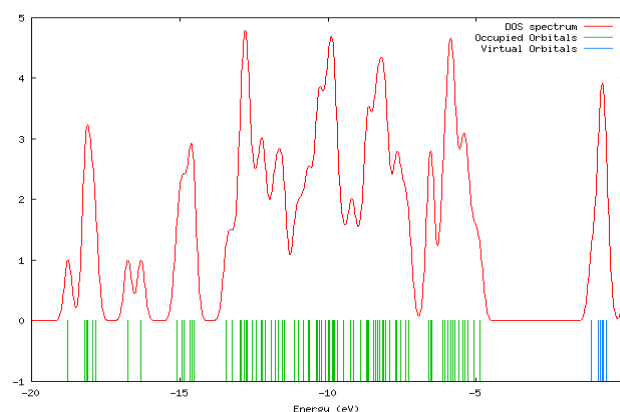


Fig. 9. DOS spectrum of ALTM

4.6. Molecular electrostatic potential

The molecular electrostatic potential, $v(r)$, at a given point r (x, y, z) in the vicinity of a molecule, is defined in terms of the interaction energy between the electrical charge generated from the molecule electrons, nuclei and a positive test charge (a proton) located at r .

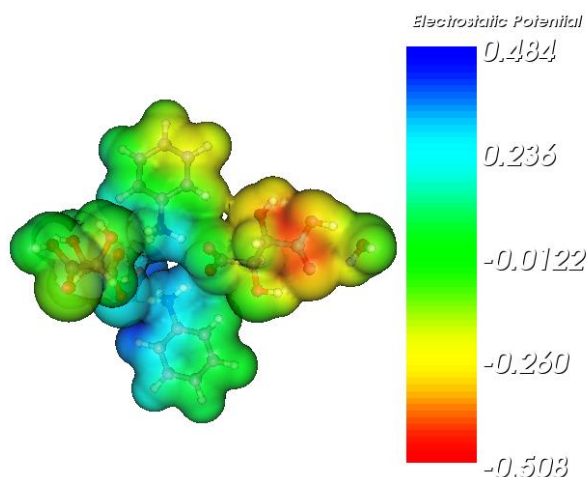


Fig. 10. Molecular Electrostatic potential map

The molecular electrostatic potential (MEP) is related to the electronic density and is a very useful descriptor for determining sites for electrophilic attack and nucleophilic reactions as well as hydrogen-bonding interactions [42,43]. Fig. 10. shows the 3D plot of molecular electrostatic potential calculated by using the optimized molecular structure at B3LYP/6-31G(d,p) level for ALTm molecule. Negative electrostatic potential are represented by red colour indicates the electrophilic reactivity; positive electrostatic potential are represented by blue colour indicates nucleophilic reactivity and green colour

represents the zero potential. The MEP map shows that the negative potential sites are on electronegative atoms as well as the positive potential sites are around the hydrogen atoms. These sites give information about the region from where the compound could have non covalent interactions

4.7. Natural bond orbital analysis

NBO method gives information about interactions in both filled and virtual orbital spaces and provides most accurate possible ‘natural Lewis structure’ and enhances the analysis of intra and intermolecular interactions. The N-H...O intermolecular interaction results obtained by second – order perturbation analysis of the Fock Matrix at B3LYP/6-31G(d,p) basis set are presented in Table 6. NBO analysis revealed that the $n(\text{O2w}) \rightarrow \sigma^*(\text{O13-H13o})$ interactions give the strongest stabilization to the ALTm system by 126.95 kJ/mol and strengthened the O13-H13o...O2w intermolecular interaction which is responsible for the complex formation. The next strongest intermolecular interaction is N1-H1...O12 carries an energy of 101.04 kJ/mol. The intermolecular interaction between aniline and tartaric molecule shows its energy value of 117.08 kJ/mol. Similarly intermolecular interaction between aniline and water gives a stabilization energy value of 99.58 kJ/mol. Thus, it is clear that N-H...O intermolecular interactions significantly influence crystal packing and vibrational frequencies of this ALTm molecule.

Table 6. Second-order perturbation theory analysis of the Fock matrix in NBO basis calculated at B3LYP/6-31G(d,p) level

Donor (i)	Acceptor (j)	$E^{(2)}$ (Kj.mol ⁻¹)	$E(j)-E(i)$ (a.u)	$F(i,j)$ (a.u)
From unit 2 to unit 1				
n_1 (O12)	$\sigma^*(\text{N1-H1N1})$	55.25	1.03	0.105
n_2 (O12)	$\sigma^*(\text{N1-H1N1})$	101.04	0.73	0.120
Within unit 2				
n_2 (O14)	$\sigma^*(\text{O15-H30})$	25.45	0.78	0.063
n_1 (O13)	$\sigma^*(\text{O16-H40})$	9.71	1.06	0.044
From unit 2 to unit 4				
n_1 (O14)	$\sigma^*(\text{O2W-H1O2})$	13.90	1.15	0.055
n_2 (O14)	$\sigma^*(\text{O2W-H1O2})$	24.45	0.73	0.060
From unit 4 to unit 2				
n_1 (O2W)	$\sigma^*(\text{O13-H13o})$	3.39	0.92	0.025
n_2 (O2W)	$\sigma^*(\text{O13-H13o})$	126.95	0.84	0.142
From unit 5 to unit 1				
n_1 (O1)	$\sigma^*(\text{N1-H2N1})$	34.91	1.05	0.085
n_2 (O1)	$\sigma^*(\text{N1-H2N1})$	117.08	0.71	0.128
From unit 5 to unit 3				
n_1 (O2)	$\sigma^*(\text{N2-H1N2})$	21.30	1.06	0.066
n_2 (O2)	$\sigma^*(\text{N2-H1N2})$	13.35	0.73	0.044
n_3 (O2)	$\sigma^*(\text{N2-H1N2})$	44.83	0.67	0.083
n_1 (O6)	$\sigma^*(\text{N2-H3N2})$	8.96	1.00	0.041
n_2 (O6)	$\sigma^*(\text{N2-H3N2})$	40.14	0.79	0.078
Within unit 5				
n_1 (O5)	$\sigma^*(\text{O6-H20})$	3.22	1.04	0.025

Donor (i)	Acceptor (j)	E ⁽²⁾ (Kj.mol ⁻¹)	E(j)-E(i) (a.u)	F(i,j) (a.u)
n ₂ (O5)	σ*(O6 – H20)	21.01	0.75	0.055
n ₂ (O3)	σ*(O5 – H10)	4.39	0.80	0.027
From unit 5 to unit 6				
n ₁ (O2)	σ*(O1W – H1O1)	25.32	1.11	0.073
n ₂ (O2)	σ*(O1W – H1O1)	60.19	0.77	0.096
n ₃ (O2)	σ*(O1W – H1O1)	14.94	0.72	0.049
From unit 6 to unit 1				
n ₁ (O1W)	σ*(N1– H3N1)	2.72	0.89	0.022
n ₂ (O1W)	σ*(N1– H3N1)	99.58	0.84	0.126

4.8. Hyperpolarizability calculation

The quadratic dependence of the second harmonic green light intensity (I_{2ω}) on the intensity of infrared exciting beam (I_ω) for polycrystalline sample of ALTM is calculated. This result can be compared with potassium dihydrogen phosphate and it is found that ALTM is 0.45 times that of KDP [44]. As mentioned above, this study is extended to the determination of the electric dipole moment μ_{tot}, the isotropic polarizability α_{tot} and the first hyperpolarizability β_{tot} of the title compound. It is well known that the non linear optical response of an isolated molecule in an electric field E_i(ω) can be presented as a Taylor series expansion of the total dipole moment, μ_{tot}, induced by the field:

$$\mu_{tot} = \mu_0 + \alpha_{ij}E_j + \beta_{ijk}E_jE_k + \dots \quad (8)$$

where μ₀ the permanent dipole moment, α_{ij} is the linear polarizability, and β_{ijk} is the first hyperpolarizability tensor components. The isotropic (or average) linear polarizability is defined as [45]:

$$\alpha_{tot} = \frac{\alpha_{xx} + \alpha_{yy} + \alpha_{zz}}{3} \quad (9)$$

$$\beta_{tot} = \sqrt{(\beta_{xxx} + \beta_{xyy} + \beta_{xzz})^2 + (\beta_{yyy} + \beta_{yzz} + \beta_{yxx})^2 + (\beta_{zzz} + \beta_{zxx} + \beta_{zyy})^2} \quad (12)$$

Since the values of the polarizability α_{tot} and the first hyperpolarizability β_{tot} of Gaussian 98 output are reported in atomic units (a.u.), the calculated values have been converted into electrostatic units (esu) (α: 1 a.u. = 0.1482×10⁻²⁴ esu ; β: 1 a.u. = 8.6393×10⁻³³ esu. Table 7 listed the B3LYP/6-31G(d,p) results of the electronic dipole moment μ_i (i = x, y, z), polarizability α_{ij} and the first hyperpolarizability β_{ijk} for Aniline-L-tartaric acid complex. The calculated dipole moment is equal to 3.04 D (Debye). The highest value of dipole moment is observed for component μ_y. In this direction, this value is equal to -2.23 D. For direction x and z, these values are equal to 1.33 D and 1.57 D respectively.

First hyperpolarizability is a third rank tensor that can be described by 3×3×3 matrix. The 27 components of 3 D matrix can be reduced to 10 components due to the Kleinman symmetry [46] (β_{xyy} β_{yyx}, β_{yyx} β_{yyz}, β_{yyz} β_{zyy}, ... likewise other permutations also take same value). The output from Gaussian 98 provides 10 components of this matrix as β_{xxx}, β_{xyy}, β_{xyy}, β_{yyy}, β_{xxz}, β_{xyy}, β_{yyz}, β_{xzz}, β_{zyz}, β_{zzz}, respectively. The components of the first hyperpolarizability can be calculated using the following equation [47]:

$$\beta_i = \beta_{iii} + \frac{1}{3} \sum_{i \neq j} (\beta_{ijj} + \beta_{jij} + \beta_{jji}) \quad (10)$$

Using the x, y and z components of β, the magnitude of the first hyperpolarizability tensor can be calculated by:

$$\beta_{tot} = \sqrt{(\beta_x^2 + \beta_y^2 + \beta_z^2)} \quad (11)$$

The complete equation for calculating the magnitude of β from Gaussian 98 output is given as follows:

Table 7. The electric dipole moment μ(D), the average polarizability α_{tot} (×10⁻²⁴ esu) and first hyperpolarizability β_{tot} (×10⁻³¹ esu)

μ _x	1.33	β _{xxx}	1.36
μ _y	-2.23	β _{yyy}	2.41
μ _z	1.57	β _{zzz}	2.67
μ	3.04	β _{xyy}	0.28
α _{xx}	-22.78	β _{xxz}	-8.47
α _{yy}	-26.37	β _{xxz}	17.93
α _{zz}	-31.63	β _{xzz}	-6.30
α _{xy}	0.08	β _{yyz}	-4.58
α _{xz}	-3.08	β _{yyz}	-2.80
α _{yz}	-1.18	β _{xyz}	-2.22
α _{tot}	26.92	β _{tot}	21.25

The calculated polarizability α_{tot} , is equal to $26.92 \cdot 10^{-24}$ esu. As we can see in Table 7, the calculated polarizability α_{ij} have non zero values and was dominated by the diagonal components. The first hyperpolarizability value β_{tot} of the title compound is equal to $21.25 \cdot 10^{-31}$ esu, which is 16.34 times that of urea ($1.3 \cdot 10^{-31}$ esu) [48]. The hyperpolarizability β dominated by the longitudinal components of β_{xxy} , β_{xxz} , β_{xzz} and β_{yzz} indicates on a substantial delocalization of charges in these directions. In directions of β_{xxx} , β_{yyy} , β_{zzz} , β_{xyy} , β_{xyz} , and β_{yyz} the values of components are relatively medium. In other directions, the particular components are practically equal to 0.

4.9. Phase transition

The DSC curves for ALTM recorded upon heating and cooling are displayed in Fig. 11. Differential scanning calorimetric measurements indicate clearly the occurrence of the phase transition of the first order approximately at 346K and 408 K for heating and cooling respectively. The energetic effects are 9.34 J/g and 5.82 J/g for first heating and second cooling, respectively. During second heating and third cooling the energetic effects were 2.90 J/g and 3,14 J/g, respectively. It is worthwhile mentioning here that during second run, peak was shifted and the energetic effects were smaller.

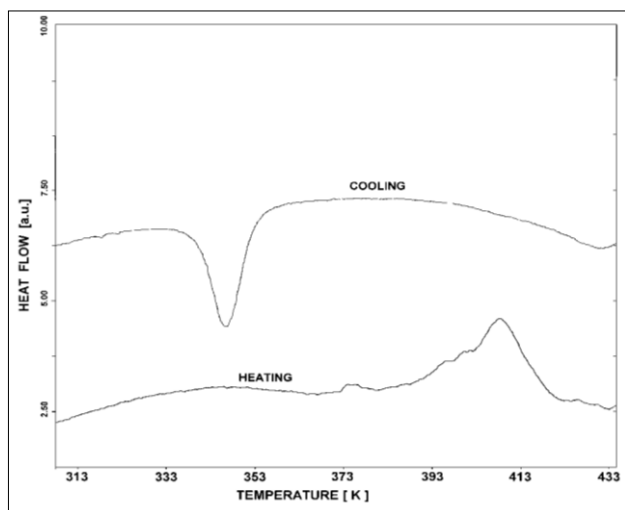


Fig. 11. DSC traces of ALTM

5. Conclusion

Single crystals of anilinium l-tartrate monohydrate (ALTM) have been grown from slow solvent evaporation technique. Single crystal X-ray diffraction studies confirm the monoclinic crystal system with non-centrosymmetric space group P21. The geometry optimization has been carried out using B3LYP /6-31G(d,p) basis set. FT-IR and FT-Raman spectra have been recorded. Internal vibrations of anilinium cations, tartrate anions and vibrations of hydrogen bonds have been identified and detailed vibrational assignments were presented. The aniline molecule occurs in studied crystal is monoprotonated with

NH₃ residue and tartaric acid molecule is slightly distorted. The obtained vibrational spectra are in full agreement with the structure obtained by X-ray experiments and the values obtained by B3LYP /6-31G(d,p) basis set. NBO analysis reflects the charge transfer interaction takes place within the molecule. The HOMO – LUMO energy gap is calculated as 3.78eV and global chemical reactivity descriptors of compounds such as hardness, chemical potential, softness, electro negativity and electrophilicity index has also been calculated. Molecular electrostatic potential predicts the most reactive part in the molecule. DSC studies confirm the phase transition approximately at 346K and 408 K for heating and cooling respectively. ALTM crystal exhibits second order nonlinear optical properties and its efficiency is 0.45 times that of KDP.

Supplementary material

Full crystallographic data (cif file) relating to the crystal structure have been deposited with Cambridge Crystallographic Data centre as CCDC 1024780. Copies of this information can be obtained free of charge from the Cambridge Crystallographic Data Centre, 12 Union Road, Cambridge CB2 1Ez. UK (Tel: +44(0) 1223 762911; email:deposit@ccdc.cam.ac.uk; <http://www.ccdc.cam.ac.uk>)

References

- [1] D. S. Chemla, J. Zyss (Eds.), Nonlinear Optical Properties of Organic Molecules and Crystals, Vol. 1 and 2, Academic Press, New York, 1987.
- [2] H. O. Marcy, M. J. Rosker, L. F. Warren, P. H. Cunningham, C. A. Thomas, L. A. Deloach, S. P. Velsco, C. A. Ebbers, J. H. Liao, M. U. Kanatzidis, *Opt. Lett.* **20**, 252 (1995).
- [3] S. S. Gupte, A. Marcarno, D. Pradhan, C. F. Desai, N. J. Melikechi, *Appl. Phys.* **89**, 4939 (2001).
- [4] T. Pal, T. Kar, G. Bocelli, L. Rigi, *Cryst. Growth Des.* **3**, 13 (2003).
- [5] S. Natarajan, S.A. Martin Britto, E. Ramachandran, *Cryst. Growth Des.* **6**, 137 (2006).
- [6] G. Ramesh Kumar, S. Gokul Raj, R. Mohan, R. Jeyavel, *Cryst. Growth Des.* **6**, 1308 (2006).
- [7] N. Vijayan, R. Remesh Babu, R. Gopalakrishnan, P. Ramasamy, M. Ichimura, M. Palanichamy, *J. Crystal Growth* **273**, 564 (2005).
- [8] V. Subhashini, S. Ponnusamy, C. Muthamizhchelvan, *Spectrochim. Acta Cryst. A* **87**, 265 (2012).
- [9] R. V. Krishnakumar, M. Nandhini, S. Natarajan, *Acta Cryst. C* **57**, 165 (2001).
- [10] M. Subha Nandhini, R. V. Krishnakumar, S. Natarajan, *Acta Cryst. C* **57**, 423 (2001).
- [11] M. K. Marchewka, J. Baran, A. Pietraszko, A. Haznar, S. Debrus, H. Ratajczak, *Solid State Sci.* **5**, 509 (2003).
- [12] M. K. Marchewka, H. Ratajczak, *J. Nonlin. Opt. Phys.* **12**, 113 (2003).

- [13] J. Shen, J. Zheng, Y. Che, B. Xi, *J. Cryst. Growth* **257**, 136 (2003).
- [14] C. T. Yan, T. S. Shih, J. F. Fen, *Talanta* **64**, 650 (2004).
- [15] H. L. Wang, F. Huang, A. G. Mac Diamid, Y. Z. Wang, D. D. Gebler, A. J. Epstein, *Synth. Met.* **78**, 33 (1996).
- [16] A. Ben Ahmed, N. Elleuch, H. Feki, Y. Abid, C. Minot, *Spectrochim. Acta Part A* **79**, 554 (2011).
- [17] A. M. Petrosyan, R. P. Sukiasyan, H. A. Karapetyan, M. Yu. Antipin, R. A. Apreyan. *J. Cryst. Growth* **275**, 1927 (2005).
- [18] M. K. Marchewka, S. Debrus, A. Pietraszko, A. J. Barnes, H. Ratajczak, *J. Mol. Struct.* **656**, 265 (2003).
- [19] M. Drozd, M. K. Marchewka, *Spectrochim. Acta A* **64**, 6 (2006).
- [20] KUMA Diffraction, KM4/CCD Users' Guide, Version 1.169 (Release April, 2000), Wrocław, Poland.
- [21] G. M. Sheldrick, SHELXTL—Program System, Siemens Analytical XRay Instruments, Inc., Madison, WI, 1990.
- [22] G. M. Sheldrick, SHELXL-97, Program for the Solution and Refinement of Crystal Structures, University of Goettingen, Goettingen, 1997.
- [23] S. K. Kurtz, T. T. Perry, *J. Appl. Phys.* **39**, 3798 (1968).
- [24] M. J. Frish, G. W. Trucks, H. B. Schlegel, G. E. Scuseria, M. A. Robb, J. R. Cheeseman, V. G. Zakrzewski, J. A. Montgomery, J. R. E. Stramann, J. C. Burant, S. Dapprich, J. M. Millam, A. D. Daniels, K. N. Kudin, M. C. Stain, O. Farkas, J. Tomasi, V. Barone, M. Cossi, R. Cammi, B. Mennucci, C. Pomelli, C. Adamo, S. Clifford, J. Ochterski, G. A. Petersson, P. Y. Agula, Q. Cui, K. Morkuma, D. K. Malick, A. D. Rabuck, K. Raghavachari, J. B. Foresman, J. Cioslowski, J. V. Ortiz, A. G. Baboul, B. B. Stefanov, G. Liv, A. Liashenko, P. Piskorz, I. Komaromi, R. Comperts, R. L. Martin, D. J. Fox, T. Keith, M. A. Al-Laham, C. Y. Peng, A. Nanayakkaray, M. Challacombe, P. M. W. Gill, B. Johnson, W. Chen, M. W. Wang, J. L. Andres, C. Gonzalez, M. Head-Gordon, E. S. Replogle, J. A. Pople, Gaussian 98, Revision A.9, Gaussian, Inc., Pittsburg Pa, 1998.
- [25] G. Rauhut, P. Pulay, *J. Phys. Chem.* **99**, 3093 (1995).
- [26] P. Flukiger, H. P. Luhti, S. Portmann, J. Weber, Molekel 4.2, Swiss Center for Scientific Computing, Manno, Switzerland, 2000-2002.
- [27] R. M. Silverstein, F. X. Webster, *Spectrometric Identification of Organic Compounds*, Sixth Ed., Wiley 1998, Chapter 3, pp. 102.
- [28] Norman Sheppard, University of East Anglia, Norwich, UK, The historical development of experimental techniques in vibrational spectroscopy, John Wiley & Sons Ltd, 2002, 1-4484.
- [29] J. Swaminathan, M. Ramalingam, V. Sethuraman, N. Sundaraganesan, S. Sebastian, *Spectrochim. Acta A* **73**, 593 (2009).
- [30] N. Sundaraganesan, H. Umamaheswari, B. Dominic Joshua, C. Meganathan, M. Ramalingam, *J. Mol. Struct. (Theochem)* **850**, 84 (2008).
- [31] Douglas M. Hudgins, C. W. Bauschlicher, Scott A. Sandford, *Astrophys. J.* **614**, 770 (2004).
- [32] M. Silverstein, G. Clayton Basseler, C. Morill, *Spectrometric Identification of Organic Compounds*, Wiley, New York, 1981.
- [33] Frontier Fleming, *Orbitals and Organic Chemical Reactions*, Wiley, London, 1976.
- [34] T. Karakurtm M. Dincer, A. Cetin, M. Sekera, *Spectrochim. Acta* **77A**, 189 (2010).
- [35] R. G. Parr, L. V. Szentpaly, S. J. Liu, *Am. Chem. Soc.* **121**, 1922 (1999).
- [36] R. Parthasarathi, J. Padmanabhan, V. Subramanian, B. Maiti, P. K. Chattaraj, *J. Phys. Chem. A* **107**, 10346 (2003).
- [37] S. Renuga, S. Muthu, *Spectrochimica Acta Part A: Molecular and Biomolecular Spectroscopy* **118**, 702 (2014).
- [38] R. Hoffmann, *Solids and Surfaces: A Chemist's View of Bonding in Extended Structures*, VCH Publishers, New York, 1988.
- [39] J. G. Malecki, *Polyhedron* **29**, 1973 (2010).
- [40] N. M. O'Boyle, A. L. Tenderholt, K. M. Langner, *J. Comp. Chem.* **29**, 839 (2008).
- [41] M. Chen, U.V. Waghmare, C.M. Friend, E. Kaxiras, *J. Chem. Phys.* **109**, 6680 (1998).
- [42] S. Sebastin, N. Sundaraganesan, *Spectrochim. Acta A* **75**, 941 (2010).
- [43] E. Scrocco, J. Tomasi, *Adv. Quantum Chem.* **11**, 115 (1978).
- [44] H. Ratajczak, J. Baran, S. Debrus, *Bull. Pol. Acad. Sci. Chem.* **49**, 261 (2001).
- [45] H. Alyar, Z. Kantarci, M. Bahat, E. Kasap, *J. Mol. Struct.* **516**, 834 (2007).
- [46] D. A. Kleinman, *Phys. Rev.* **126**, 1977 (1962).
- [47] H. Unver, A. Karakas, A. Elmali, *J. Mol. Struct.* **702**, 49 (2004).
- [48] M. Adant, I. Dupuis, L. Bredas. *Int. J. Quantum. Chem.* **56**, 497 (2004).

*Corresponding author: marchewka.mariusz578@gmail.com;
kanagathaara@gmail.com